

A multi-patch nonsingular isogeometric boundary element method using trimmed elements

Yingjun Wang¹ · David J. Benson¹ · Attila P. Nagy²

Received: 17 April 2015 / Accepted: 29 April 2015 / Published online: 19 May 2015
© Springer-Verlag Berlin Heidelberg 2015

Abstract One of the major goals of isogeometric analysis is direct design-to-analysis, i.e., using computer-aided design (CAD) files for analysis without the need for mesh generation. One of the primary obstacles to achieving this goal is CAD models are based on surfaces, and not volumes. The boundary element method (BEM) circumvents this difficulty by directly working with the surfaces. The standard basis functions in CAD are trimmed nonuniform rational B-spline (NURBS). NURBS patches are the tensor product of one-dimensional NURBS, making the construction of arbitrary surfaces difficult. Trimmed NURBS use curves to trim away regions of the patch to obtain the desired shape. By coupling trimmed NURBS with a nonsingular BEM, the formulation proposed here comes close achieving the goal of direct design to analysis. Example calculations demonstrate its efficiency and accuracy.

Keywords Isogeometric analysis · Boundary element method · Nonsingular integration · Trimmed elements · Quadrature design

1 Introduction

Isogeometric analysis (IGA) [16,33] combines the variational framework of the finite element method (FEM) [34] with the basis functions used in computer-aided design

(CAD), e.g., nonuniform rational B-splines (NURBSs) [56]. This methodology has been successfully applied to a variety of domains, e.g., structural vibration [17], electromagnetics [15], fluids [1,7], fluid–structure interaction [6,8,32], phase field analysis [13,43], contact [48,72], fracture [18], shape optimization [2,57], topology optimization [19,67], cables and shells [10–12,58].

Building complicated geometries with the restrictive tensor product structure of NURBS is every bit as difficult as building them for logically regular meshes used by finite difference methods. In fact, the difficulty of meshing complicated geometries is one reason why finite difference methods were replaced by the FEM with its unstructured meshes. A natural direction of research is therefore the development of basis functions that have the smoothness of NURBS and the unstructured meshes of piecewise continuous polynomials. Among the most popular candidate basis functions are T-splines [66], which have been used successfully in IGA [5,63,64]. Competitors to T-splines for analysis include PHT-splines [53,75], hierarchical B-splines or NURBS [62,73] and Powell–Sabin splines [30,31] among many others.

Trimmed NURBS are the most common approach for creating complicated geometries in CAD. Curves define the domain to be kept on a NURBS patch, and the remainder is trimmed away and discarded. A state-of-the-art large-scale CAD model may be built from dozens or hundreds of trimmed surfaces that are connected along non-matching boundaries and trimming curves [61]. Since the trim curves can cut through the elements in an arbitrary manner, the geometries of the trimmed elements may be irregular, making their implementation challenging within a traditional finite element framework.

Kim et al. [37] first presented trimmed surfaces based in a NURBS-enhanced FEM [68]. The trimmed elements are decomposed into simple geometries, i.e., triangles or

✉ David J. Benson
dbenson@ucsd.edu

¹ Department of Structural Engineering, University of California, San Diego, La Jolla, USA

² Livermore Software Technology Corporation, Livermore, USA

quadrilaterals with at most one trimmed curve side, and a projection scheme is used to map the simple geometries to regular geometries, and standard quadrature rules are used for integration. Later, Kim et al. [38,67] improved their method and applied it to topology optimization. Complicated elements may be generated when they are trimmed by multiple curves, and a quadtree refinement was used to recursively refine them, greatly increasing the number of integration points.

Ruess et al. [60] used a reduced integration approach to trimmed elements for a finite cell method. They used quadtree refinement to subdivide trimmed elements. Their modified Gauss quadrature used only the Gauss points interior to the trimmed elements. This method increases the number of integration points, and the finite cell method usually cannot exactly represent the smooth boundary of the geometry. Wang et al. [77] classified the types of trimmed elements and proposed different integration schemes to avoid using local quadtree refinement, but their method adds the complexity of identifying the different types of trimmed elements and requires the decomposition of the pentagonal and hexagonal trimmed elements into elements with simpler shapes.

Nagy and Benson [51] recently proposed an algorithm based on optimization to construct efficient quadrature rules for trimmed elements of arbitrary shape and topology. The integration rule is unique to a trimmed element and it is optimal within the trimmed domain up to a predefined tolerance. This method is used here for the numerical integration of trimmed elements.

CAD uses a boundary representation for volumes, i.e., volumes are defined in terms of their exterior surfaces, and these surfaces are defined in terms of trimmed NURBS that are usually not compatible in terms of their knot vectors. Generating a three-dimensional volumetric model from the CAD surface definitions has been a challenge [26,46]. The boundary element method (BEM) [3,4], unlike traditional FEMs, only requires surface meshes for the analysis of solids, making it attractive for IGA [25,55,65,69,70]. Although combining BEM with IGA offers many opportunities, it still faces the usual challenge in BEM of integrating singular and nearly singular integrals and the usual challenge of using NURBS in IGA for the analysis of complicated topologies.

The fundamental solutions in the BEM usually contain $O(1/r^\alpha)$ terms resulting in nearly singular and singular integrals that cannot be accurately evaluated by standard Gaussian quadrature. One approach uses special techniques to accurately evaluate these integrals, e.g., analytical methods [27,28], degenerate mapping methods [41], radial integration methods [22,23] and non-linear transformation methods [71,81] for singular integrals, and domain division methods [9,24], semi-analytical and analytical methods [54,82] and

a series of transformation methods [35,49,50,79,80] for the nearly singular integrals. These methods only work for simple shapes such as triangular and quadrilateral elements, and therefore they cannot be used in irregular trimmed elements. The other approach constructs weakly-singular or nonsingular boundary integral equations (BIEs) by a series of algebraic operations, so that standard quadrature rules can be used for element integration. Rizzo and Shippy [59] first presented a weakly-singular form by expressing the free term coefficient matrix C_{ij} obtained through the rigid body translation solutions on the BIE. Liu et al. [44,45,47] proposed several identities for the fundamental solutions and applied them to weakly-singular and nonsingular BEMs. In recent years, a new nonsingular BEM was developed by Klaseboer et al. [39,40]. It was extended to single-patch IGA for 3D Stokes flow by Heltai et al. [29] to demonstrate the validity of the nonsingular IGABEM.

In this paper, we present a nonsingular IGABEM based on a previous nonsingular BEM [47], and combine it with the quadrature rules for trimmed elements [51] to implement a multi-patch nonsingular IGABEM with trimmed elements. The paper is organized as follows: in Sect. 2, the use of trimmed NURBS in IGA is briefly reviewed. The numerical integration of trimmed isogeometric elements is summarized in Sect. 3. The nonsingular IGABEM is presented in Sect. 4. Numerical examples are shown in Sect. 5. Finally, conclusions and future research are discussed in Sect. 6.

2 IGA using trimmed NURBS

Trimmed NURBS surfaces, which consist of untrimmed NURBS surfaces and trimming curves, play an important role in CAD systems. Complex geometries are typically composed of several trimmed surfaces since adding features (e.g., fillets and holes) to a geometric model are commonly done by trimming in CAD software. Note that the parameterization of NURBS surfaces remains unchanged, and the parts of the surface outside of the trim curves are simply not displayed. In order to identify which part is trimmed, an orientation rule for the trimming curves is defined, e.g., the trimmed region is to the right of the direction of the increasing knot values and the remaining region is to the left [38].

In general, NURBS surfaces and trimming curves are defined by different parameter sets (ξ, η) and (τ) , respectively. For example, a NURBS surface $S(\xi, \eta)$ and a trimming curve $C(\tau)$ are described as

$$S(\xi, \eta) = \sum_{i=1}^n \sum_{j=1}^m N_{i,j}(\xi, \eta) \mathbf{P}_{i,j}, \quad (1)$$

$$C(\tau) = \sum_{k=1}^m N_k(\tau) \mathbf{P}_k, \quad (2)$$

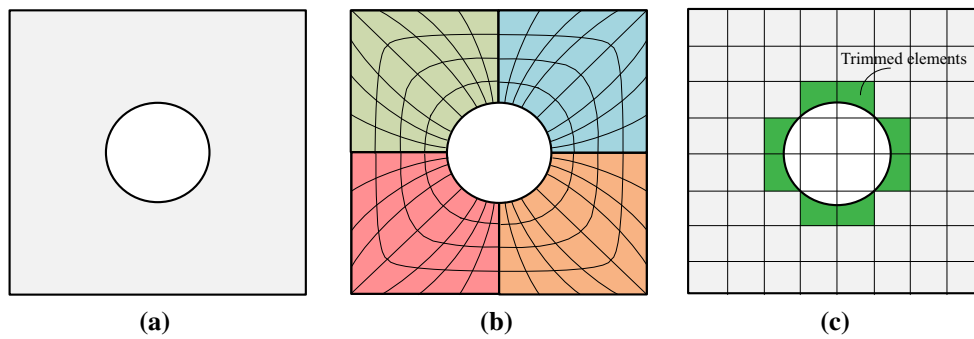


Fig. 1 Different models in IGA: **a** CAD model, **b** multi-patch analysis suitable model and **c** trimmed NURBS model

where $N_{i,j}(\xi, \eta)$ and N_k are the rational basis functions of the surface and the curve, respectively, and $\mathbf{P}_{i,j}$ and \mathbf{P}_k are the corresponding control points. In order to describe a trimmed surface, the curve is expressed in terms of underlying surface as

$$S_c(\xi(\tau), \eta(\tau)) = \sum_{i=1}^n \sum_{j=1}^m N_{i,j}(\xi(\tau), \eta(\tau)) \mathbf{P}_{i,j}. \quad (3)$$

Since there is no analytical relationship between parameter sets (ξ, η) and (τ) , a proper parametric representation of the curve in the parametric domain of the underlying NURBS surface is not possible.

In conventional IGA with NURBS patches, a model with complex topology is manually divided into multiple tensor product patches. For example, the analysis suitable model for the geometric model in Fig. 1a is constructed of four NURBS patches as shown in Fig. 1b. IGA requires a certain level of continuity to be maintained between adjacent patches (e.g., common control points), but it is not easy to implement this requirement in CAD systems. Moreover, the continuity between the adjacent elements of neighboring patches is reduced to C^0 . If the analysis model uses the trimming operations as illustrated Fig. 1c, the continuity problem can be solved. However, this trimmed model introduces the challenge of integrating the trimmed elements, a key issue for IGA based on trimmed NURBS.

3 Integration on the trimmed elements

There are a number of ways of performing quadrature on a trimmed NURBS surface. Most of them are efficient enough for problems where the integration is only performed once, e.g., a linear structural analysis where each element is integrated only once. In BEM, the integration over an element is performed roughly once for every node in the problem, and therefore efficiency is critical. This concern for efficiency motivated the choice of using a highly efficient integration method [51] for the repetitive evaluation of element inte-

grals in IGA applications using explicit time integration for structural dynamics. The method is summarized here; for additional details, the interested reader is referred to [51].

3.1 Function space and the moment fitting equations

Basic splines are piecewise polynomials constructed as a weighted sum of monomials,

$$B(\xi) = \sum_{i=1}^m c_i f_i(\xi), \quad (4)$$

where $\xi = (\xi_1, \dots, \xi_n)$ are the parametric coordinates in n dimensions, and c_i and f_i are the i th coefficient and monomial. The function space \mathcal{F} for the tensor product spline polynomials consists of the set of all monomials $\xi_1^r \xi_2^s$ such that $0 \leq r, s \leq p$, where p is the degree of the spline in one dimension.

The standard form of a numerical integration formulation may be written as

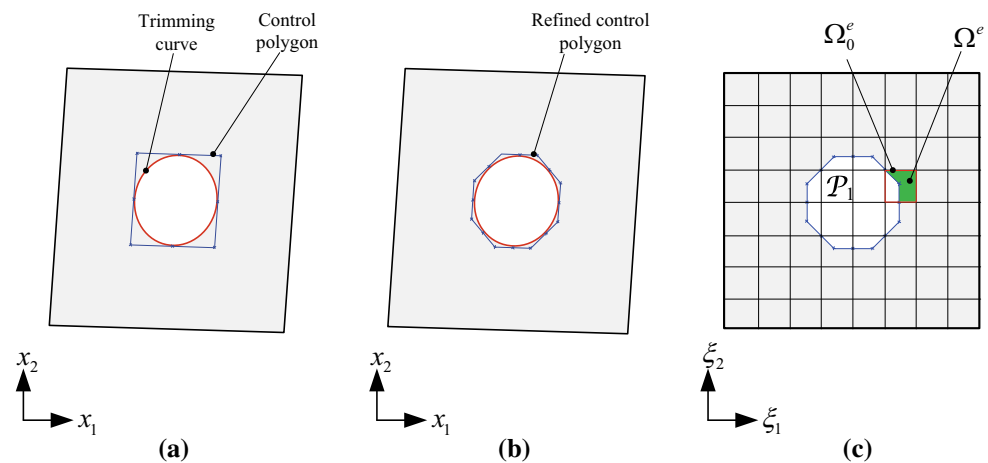
$$\int_{\Omega} f(\xi) d\xi \approx \sum_{i=1}^m w_i f(\xi_i), \quad (5)$$

where $\Omega \in \mathbb{R}^n$ is the domain of integration, and f is the integrand. The symbols ξ_i and w_i denote the i th quadrature point and the weight.

When a predefined function space $\mathcal{F}(\Omega)$ is chosen, integration rules are constructed to satisfy Eq. (5) for all functions $f_j \in \mathcal{F}$ with $j = 1, \dots, m$. For the purpose of this, we need to solve the set of moment-fitting equations that are linear in the weights and nonlinear in the locations of the quadrature points ξ_i

$$\begin{pmatrix} \int_{\Omega} f_1(\xi) d\xi \\ \int_{\Omega} f_2(\xi) d\xi \\ \vdots \\ \int_{\Omega} f_n(\xi) d\xi \end{pmatrix} = \begin{bmatrix} f_1(\xi_1) & f_1(\xi_2) & \cdots & f_1(\xi_m) \\ f_2(\xi_1) & & \ddots & \\ \vdots & & & \\ f_n(\xi_1) & \cdots & & f_n(\xi_m) \end{bmatrix} \begin{pmatrix} w_1 \\ w_2 \\ \vdots \\ w_m \end{pmatrix}. \quad (6)$$

Fig. 2 Approximation of the trimmed domain: domain with **a** initial and **b** refined trimming curves in the physical space, and **c** the approximated trimmed elements in the parametric space



The above relation may be described in a compact form as

$$\mathbf{g}(\mathbf{x}) = \mathbf{f}_c - \mathbf{f}(\mathbf{x}) = \mathbf{0}, \quad (7)$$

where the \mathbb{R}^n vectors \mathbf{f}_c and \mathbf{f} represent the left and right hand side terms in Eq. (6). Moreover, the symbol $\mathbf{x} \in \mathbb{R}^{m(n+1)}$ designates the collection of quadrature points and corresponding weights, i.e., $\mathbf{x} = \{\mathbf{x}_i | i = 1, \dots, m\}$ where $\mathbf{x}_i = (\xi_i^1, \dots, \xi_i^n, w_i)$ is referred to as a design point.

3.2 The domain of trimmed elements

A trimmed element may consist of several curves intersecting the four edges of the element and each other. To simplify the computational geometry, the domain of a trimmed element is approximated as a polytope in the parametric space generated by a two step process. In the first step, h -refinement is applied to the trimming curves, and improves the approximation quality of the respective control polygons. Note that as the refinement becomes finer, the control polygon moves closer to the curve. In practice, knot insertion can be performed such that the control polygon associated with the refined curve approximates the curve itself up to machine tolerance. In the second step, the control polygons are pulled back to the parametric space using the point inversion (projection) algorithm [56]. Assuming an image of the control polygon in the parametric space is closed (noted as \mathcal{P}_i), the domain of a trimmed element Ω^e is easily defined by taking the difference of the untrimmed knot span Ω_0^e and the trimming polygons as

$$\Omega^e = \Omega_0^e \setminus (\cup_i \mathcal{P}_i). \quad (8)$$

A simple two-dimensional example is illustrated in Fig. 2. For improved visibility, the trimming curve is only modestly refined here.

3.3 Quadrature design on trimmed elements

Once the trimmed elements are represented as Eq. (8), the left hand side terms in Eq. (7) are evaluated using Lasserre's theorems [42] to provide reference values for the integrals of the monomials when the element domain is a convex polytope. If the element domain is non-convex, the original polytope may be partitioned into convex sub-polytopes, or convex hull generation and vertex elimination may be used to compute the integrand [51].

Given an initial set of quadrature points and weights, the algorithm approximates the solution of Eq. (7) in the least squares sense. The quadrature points in the minimum norm solution are classified and the point with the lowest rank is eliminated. This reduced set of points is used to reinitialize the non-linear equation solver in the next iteration. The process continues until the integration rule with the lowest number of points is found that satisfies the moment fitting equation up to a predefined tolerance. For more details of the algorithm, the reader is referred to [51].

4 Nonsingular IGABEM for three-dimensional elastostatics

4.1 Boundary integral equation

This section provides a brief review of the standard BIEs to establish notation; a complete presentation with their derivation may be found in any textbook on BEM, e.g., [9]. In this work, the summation convention is used for repeated lowercase Latin indices unless explicitly indicated otherwise.

For a physical domain with a boundary Γ discretized into M elements, assuming each element contains A nodes and the body forces are zero, the discrete BIE of elastostatics associating to a source point (i.e., collocation point) \mathbf{s} may be formulated as

$$\begin{aligned}
 C_{ij}(s)u_j(s) + \sum_{e=1}^M \sum_{\alpha=1}^A u_j^{e\alpha} H_{ij}^{e\alpha}(s, \mathbf{x}) \\
 = \sum_{e=1}^M \sum_{\alpha=1}^A t_j^{e\alpha} G_{ij}^{e\alpha}(s, \mathbf{x}), \tag{9}
 \end{aligned}$$

and

$$G_{ij}^{e\alpha}(s, \mathbf{x}) = \int_{\Gamma_e} U_{ij}(s, \mathbf{x}) N_{e\alpha}(\mathbf{x}) d\Gamma(\mathbf{x}), \tag{10}$$

$$H_{ij}^{e\alpha}(s, \mathbf{x}) = \int_{\Gamma_e} T_{ij}(s, \mathbf{x}) N_{e\alpha}(\mathbf{x}) d\Gamma(\mathbf{x}), \tag{11}$$

where \mathbf{x} is a field point, i.e., integration point, $u_j^{e\alpha}$ and $t_j^{e\alpha}$ are the j th component of the displacement and traction of the α th node of element e , $N_{e\alpha}(\mathbf{x})$ is the shape function of the α th node of element e at point \mathbf{x} , and $C_{ij}(s)$ is the free term coefficient depending on the boundary geometry at point s . $U_{ij}(s, \mathbf{x})$ and $T_{ij}(s, \mathbf{x})$ are the fundamental solution kernels for 3D elastostatic problems,

$$U_{ij}(s, \mathbf{x}) = \frac{1}{16\pi\mu(1-\nu)r} \{ (3-4\nu)\delta_{ij} + r_i r_j \}, \tag{12}$$

$$\begin{aligned}
 T_{ij}(s, \mathbf{x}) = -\frac{1}{8\pi(1-\nu)r^2} \left\{ \frac{\partial r}{\partial \mathbf{n}} [(1-2\nu)\delta_{ij} + 3r_i r_j] \right. \\
 \left. - (1-2\nu)(r_i n_j - r_j n_i) \right\}, \tag{13}
 \end{aligned}$$

where $r = |\mathbf{x} - s|$, $r_i = \frac{\partial r}{\partial x_i}$, n_i is the i th component of the unit outward normal \mathbf{n} , ν is Poisson’s ratio, μ is shear modulus, and δ_{ij} is the Kronecker delta.

Applying Eq. (9) at each source point on the boundary and merging the coefficients $H_{ij}^{e\alpha}(s, \mathbf{x})$ and $C_{ij}(s)$, the matrix form of the BIE system can be assembled as

$$\mathbf{H}\mathbf{u} = \mathbf{G}\mathbf{t}. \tag{14}$$

Assigning all the unknowns in \mathbf{u} and \mathbf{t} to the left hand side, and the known ones to the right hand side, Eq. (14) may be reassembled into the linear algebraic equation system

$$\mathbf{A}\mathbf{q} = \mathbf{b}, \tag{15}$$

where \mathbf{q} is the vector of unknown u and t components, \mathbf{A} is the associated collection of coefficients from \mathbf{H} and \mathbf{G} , and \mathbf{b} is the product of the known u and t components and their corresponding coefficients in \mathbf{H} and \mathbf{G} .

The IGABEM differs from the conventional BEM in that the summation $\sum_{\alpha=1}^A$ in Eq. (9) involves the control points instead of nodes. Using the parametric coordinate system (ξ, η) , the displacements and tractions of a point $\mathbf{x}(\xi, \eta)$ are evaluated from the control point values,

$$u_i(\xi, \eta) = \sum_{\alpha=1}^A N_\alpha(\xi, \eta) u_i^\alpha, \tag{16}$$

$$t_i(\xi, \eta) = \sum_{\alpha=1}^A N_\alpha(\xi, \eta) t_i^\alpha, \tag{17}$$

where $N_\alpha(\xi, \eta)$ is the basis function of the α th control point evaluated at (ξ, η) .

4.2 Nonsingular IGABEM

4.2.1 Nonsingular BIE

The free term coefficient $C_{ij}(s)$ in Eq. (9) may be written as [45]

$$C_{ij}(s) = -\sum_{e=1}^M \int_{\Gamma_e} T_{ij}(s, \mathbf{x}) d\Gamma(\mathbf{x}). \tag{18}$$

Substituting the above equation into Eq. (9), the following weakly-singular form of the BIE is obtained

$$\begin{aligned}
 \sum_{e=1}^M \int_{\Gamma_e} T_{ij}(s, \mathbf{x}) [u_j(\mathbf{x}) - u_j(s)] d\Gamma(\mathbf{x}) \\
 = \sum_{e=1}^M \int_{\Gamma_e} U_{ij}(s, \mathbf{x}) t_j(\mathbf{x}) d\Gamma(\mathbf{x}), \tag{19}
 \end{aligned}$$

where $u_j(\mathbf{x})$ and $t_j(\mathbf{x})$ are the j th component of the displacement and traction at field point \mathbf{x} , which is evaluated by Eqs. (16) and (17).

Applying the fourth identity for the elastostatic problems [47] into Eq. (19), the resulting formulation is

$$\begin{aligned}
 \sum_{e=1}^M \int_{\Gamma_e} T_{ij}(s, \mathbf{x}) u_{j,k}(s) (x(\mathbf{x})_k - x(s)_k) d\Gamma(\mathbf{x}) \\
 = E_{j k p q} u_{j,k}(s) \sum_{e=1}^M \int_{\Gamma_e} U_{ip}(s, \mathbf{x}) n_q(\mathbf{x}) d\Gamma(\mathbf{x}), \tag{20}
 \end{aligned}$$

where $E_{j k p q}$ is the elastic modulus tensor, $n_q(\mathbf{x})$ is the q th component of the outward normal at \mathbf{x} , and $x(\mathbf{x})_k$ and $x(s)_k$ are the k th components of the physical coordinates at \mathbf{x} and s .

The nonsingular form of the BIE are obtained by subtracting Eq. (20) from Eq. (19),

$$\begin{aligned}
 \sum_{e=1}^M \int_{\Gamma_e} T_{ij}(s, \mathbf{x}) [u_j(\mathbf{x}) - u_j(s) \\
 - u_{j,k}(s) (x(\mathbf{x})_k - x(s)_k)] d\Gamma(\mathbf{x}) \\
 = \sum_{e=1}^M \int_{\Gamma_e} U_{ij}(s, \mathbf{x}) [t_j(\mathbf{x}) - E_{j k p q} u_{j,k}(s) n_q(\mathbf{x})] d\Gamma(\mathbf{x}). \tag{21}
 \end{aligned}$$

Due to $E_{jkpq}u_{j,k} = E_{pqjk}u_{j,k} = \sigma_{pq}$ and $t_j = \sigma_{jk}n_k$, the above formulation can be expressed as

$$\begin{aligned} & \sum_{e=1}^M \int_{\Gamma_e} T_{ij}(s, \mathbf{x}) [u_j(\mathbf{x}) - u_j(s) \\ & \quad - u_{j,k}(s) (x(x)_k - x(s)_k)] d\Gamma(\mathbf{x}) \\ &= \sum_{e=1}^M \int_{\Gamma_e} U_{ij}(s, \mathbf{x}) [\sigma_{jk}(\mathbf{x}) - \sigma_{jk}(s)] n_k(\mathbf{x}) d\Gamma(\mathbf{x}) \\ &= \sum_{e=1}^M \int_{\Gamma_e} U_{ij}(s, \mathbf{x}) [t_j(\mathbf{x}) - \sigma_{jk}(s)n_k(\mathbf{x})] d\Gamma(\mathbf{x}), \quad (22) \end{aligned}$$

where the first term and the second term are the nonsingular form of the BIE in [47], which may be seen as a second order truncation and a first order truncation of the Taylor’s series expansion at point s , i.e., $O(r^2)$ and $O(r)$ terms, respectively. But in the practical implementation, we prefer the third term to the second term, since it is easier to compute $t_j(\mathbf{x})$ than $\sigma_{jk}(\mathbf{x})$.

In the IGABEM, the key issues associated with Eq. (22) are how to evaluate $u_{j,k}(s)$ and $\sigma_{jk}(s)$ from the displacements and tractions of control points, which are derived in Appendix.

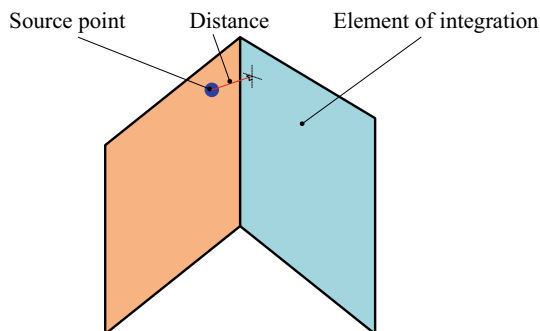


Fig. 3 An example of nearly singular integration

4.2.2 Nearly singular integration

At the sharp corners and edges of the intersecting patches, the displacements are C^0 continuous and the stresses are discontinuous, which means that the left hand side and right hand side of Eq. (22) cannot be seen as the truncations of a Taylor’s series expansion. When a source point is close to an element belonging to a different patch, the integration of the element is nearly singular since the ratio of point-element distance versus element side is very small (see Fig. 3). More details about the nearly singular integration in the BEM are available in [9,24]. Note that there is no nearly singular integration when the source point and the element belongs to the same patch in the nonsingular IGABEM.

For the untrimmed elements, the element subdivision scheme [9] is one of the most effective methods and is used herein. Figure 4a is an example that an element is divided into 16 sub-elements and 4×4 Gaussian quadrature rule is used for each sub-element. For the trimmed elements, the element subdivision scheme may be also used, but the Gauss points need to be divided into three categories based on their locations as shown in Fig. 4b, where Ω_{int} is the integration domain and Ω_{empty} is the empty domain. The integration points located completely inside Ω_{empty} are not evaluated, and the integration points on the trimming curve are evaluated but the weights are reduced to half their original value. The inspiration of the Gauss point classification comes from the work of Ruess et al. [60]. In order to improve the efficiency, the reusable intrinsic sample point algorithm [36] is used in this work.

4.2.3 Collocation

According to a comparison of different collocation methods in [46], Greville abscissae are the best choice for obtaining accurate and stable results in IGABEM, and therefore they are adopted here to design the locations of collocation points (source points). In the nonsingular IGABEM, the source point outward normal needs to be evaluated [see n in

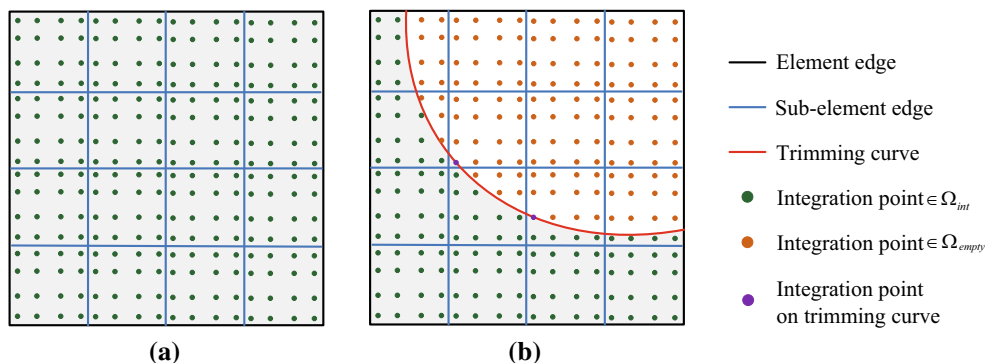


Fig. 4 Nearly singular integration schemes for a untrimmed elements and b trimmed elements

Eq. (36)], but it is not uniquely defined if the source point is at a sharp edge or corner. The methodology summarized here is developed in detail in [74].

In order to conveniently evaluate outward normals of collocation points and implement the multi-patch IGABEM, the Greville abscissae are modified by moving the edge collocation points to inside the patches. First, the initial values of the collocation points are chosen as the Greville abscissae in the parameter space along each direction of all patches as

$$\bar{\xi}_i = \frac{1}{p} (\xi_{i+1} + \xi_{i+2} + \dots + \xi_{i+p}), \quad i = 1, 2, \dots, n, \tag{23}$$

where p is the order of the NURBS basis, n is the number of control points in ξ direction. The first and the last collocation points of Eq. (23) are moved inside the patch by

$$\begin{aligned} \bar{\xi}_1 &= \bar{\xi}_1 + \beta (\bar{\xi}_2 - \bar{\xi}_1), \\ \bar{\xi}_n &= \bar{\xi}_n - \beta (\bar{\xi}_n - \bar{\xi}_{n-1}), \end{aligned} \tag{24}$$

where β ($0 < \beta < 1$) is a coefficient that defines how much the collocation points move inside the patch.

Since some control points may be shared by multiple patches but each collocation point only belongs to one patch, the number of total collocation points is usually not equal to the number of total control points when the modified Greville abscissae are used. This inequality will result in the number of BIEs being larger than the number of unknowns. To solve this problem, the equations for all the collocation points related to a single control point are merged. For example, the index relationship ($i, j, k \rightarrow m$) is set up for the three collocation points (CL_i, CL_j, CL_k) that correspond to the control point (C_m) in Fig. 5. Assume that the three BIEs in the initial assembly of Eq. (15) corresponding to the collocation points with respect to the α th direction are

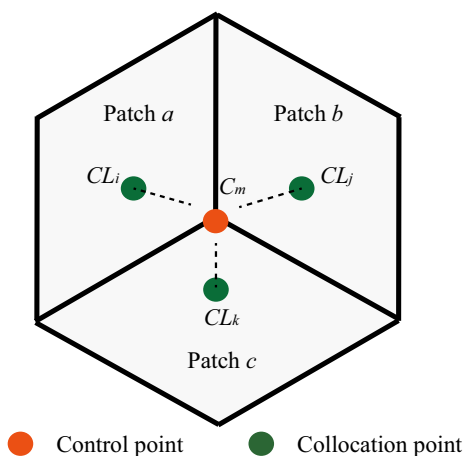


Fig. 5 An example of three collocation points versus one control point

$$\begin{aligned} A_{\bar{i}1}q_1 + A_{\bar{i}2}q_2 + \dots + A_{\bar{i}n}q_n &= b_{\bar{i}}, \\ A_{\bar{j}1}q_1 + A_{\bar{j}2}q_2 + \dots + A_{\bar{j}n}q_n &= b_{\bar{j}}, \\ A_{\bar{k}1}q_1 + A_{\bar{k}2}q_2 + \dots + A_{\bar{k}n}q_n &= b_{\bar{k}}, \end{aligned} \tag{25}$$

where $\bar{i} = 3i + \alpha, \bar{j} = 3j + \alpha, \bar{k} = 3k + \alpha$. Using the index relationship ($i, j, k \rightarrow m$), the merged BIE for the final equation system Eq. (15) is simply the average

$$\frac{1}{3} (\bar{A}_{\bar{m}1}q_1 + \bar{A}_{\bar{m}2}q_2 + \dots + \bar{A}_{\bar{m}n}q_n) = \bar{b}_{\bar{m}}, \tag{26}$$

where

$$\bar{A}_{\bar{m}p} = A_{\bar{i}p} + A_{\bar{j}p} + A_{\bar{k}p}, \quad p = 1, 2, \dots, n. \tag{27}$$

If there are Q collocation points corresponding to a control point, the number of equations in Eq. (25) should be Q and the $\frac{1}{3}$ in Eq. (26) should be replaced with $\frac{1}{Q}$.

4.2.4 Lagrange multipliers to couple intersecting surfaces

There is discontinuity along the intersection curves of the different trimmed patches, e.g., a cut with a cylindrical cutout given in Fig. 6. Taking the top square surface and the cylindrical surface as an example (see Fig. 6b), it may be observed that the control points of the two surfaces are not contiguous along their intersection (see Fig. 6c) and therefore the continuity of the displacement along the intersection is not guaranteed.

Lagrange multipliers are commonly used to impose constraints in the FEM [21, 34], and they are used here to enforce the continuity of the displacements along the intersecting trimmed NURBS curves. Assuming a point P is on a intersection curve of surfaces s_1 and s_2 , according to Eq. (16), the constraint equation of the i -component of the displacement is

$$\sum_{\alpha=1}^A N_{s_1,\alpha} (\xi_{s_1}, \eta_{s_1}) u_i^{s_1,\alpha} - \sum_{\beta=1}^B N_{s_2,\beta} (\xi_{s_2}, \eta_{s_2}) u_i^{s_2,\beta} = 0, \tag{28}$$

where A and B are the number of control points that influence point P , (ξ_{s_1}, η_{s_1}) and (ξ_{s_2}, η_{s_2}) are the parametric coordinates of P in surfaces s_1 and s_2 , and $N_{s_1,\alpha}, N_{s_2,\beta}, u_i^{s_1,\alpha}$ and $u_i^{s_2,\beta}$ are corresponding basis functions and displacements associating with the α th control point.

The computational procedure is:

- (1) Choose one of the surfaces as the master surface and equally sample points along the intersection curve in the parametric space and compute their corresponding physical points.

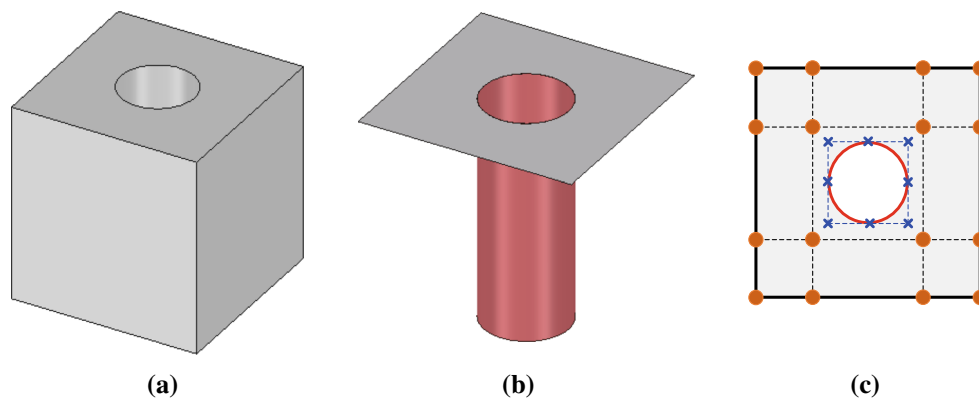


Fig. 6 A model with cylindrical cutout: **a** CAD model, **b** a pair of intersected surfaces and **c** control points on the top surface (orange dots for the square patch and blue crosses for the circle). (Color figure online)

- (2) Use the point inversion algorithm [56] to obtain the parametric coordinates of the physical points in the slave surface, and use Eq. (28) to couple the DOFs of all the sample points to obtain the equations

$$N\mathbf{u} = \mathbf{0}. \quad (29)$$

If the displacement \mathbf{u} in Eq. (29) is replaced with traction \mathbf{t} , Eq. (29) is a constraint equation on the traction.

- (3) Adding the Lagrange multipliers, collected in vector $\boldsymbol{\lambda}$, the resulting equation system is

$$\begin{bmatrix} \mathbf{A} & \mathbf{N}^T \\ \mathbf{N} & \mathbf{0} \end{bmatrix} \begin{bmatrix} \mathbf{u} \\ \boldsymbol{\lambda} \end{bmatrix} = \begin{bmatrix} \mathbf{b} \\ \mathbf{0} \end{bmatrix}, \quad (30)$$

and solving this system provides \mathbf{u} and $\boldsymbol{\lambda}$.

In Eq. (30), \mathbf{A} and \mathbf{u} correspond to \mathbf{A} and \mathbf{q} in Eq. (15). However, vector \mathbf{q} consists of the unknown displacements and tractions of the control points. If the portion of \mathbf{u} corresponding to \mathbf{N} contains both displacements and tractions, the Lagrange multiplier method may not work well because Eq. (29) becomes meaningless. This is a challenging problem which needs to be addressed in future research. Another thing that should be noted is that the Lagrange multiplier method only couples the selected points, which is just an approximation of the enforcing continuity pointwise along the entire intersection curve, but it has proven adequate as the example calculations demonstrate.

Remark 1 (The number of coupled points) Assume that A and B are the number of control points that influence the intersection curve of master surface and slave surface, respectively. Based on our experience, setting the number of coupled points in the range from $0.5\max(A, B)$ to $\max(A, B)$ gives adequate accuracy. When more coupled points are sampled, the accuracy does not increase but the efficiency is decreased. A discussion about this can be found in Sect. 5.1.

Clearly the trim curve could be used as a one-dimensional mortar “surface” in a mortar formulation [14] for tied contact. In terms of direct design-to-analysis, the trim curve does not necessarily have the appropriate number of basis functions for representing the Lagrange multiplier field accurately along the curve since it only needs to define the geometry. Given the number of issues that have to be addressed for using trimmed NURBS in BEM, the issues associated with the appropriate refinement of the trim curve for an accurate mortar formulation have been deferred to future research.

4.3 The trimming effect

The trim curves may introduce small element fragments where the values of some of the basis functions are small, e.g., the trimmed elements associating with the control point \mathbf{A} in Fig. 7. This produces a special type of error into the numerical results of the associated control point, and this is denoted the *trimming effect* here.

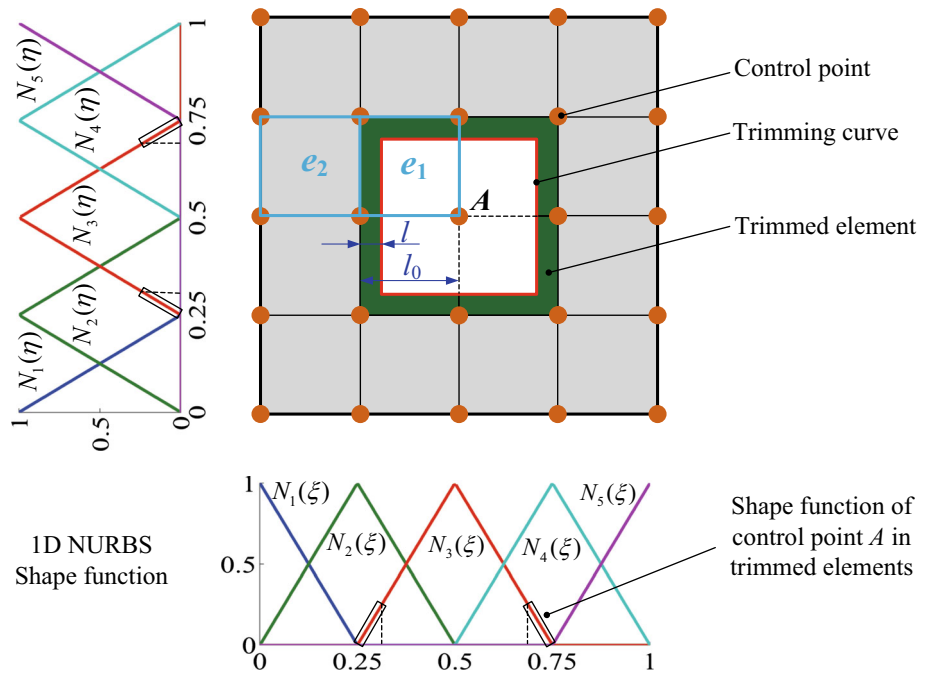
This problem is addressed by replacing the displacement field in the fragment with one from an adjacent element. Taking element e_1 in Fig. 7 as an example, the point $\mathbf{x}(\xi, \eta)$ in e_1 may be represented as

$$\phi_{e_1}(\xi, \eta) = \sum_{\alpha=1}^A N_{e_2}^{\alpha}(\xi, \eta) \phi_{e_2}^{\alpha}, \quad (31)$$

where ϕ can be the coordinates, displacements, tractions, etc. Element e_2 is an untrimmed neighbor element of element e_1 (see Fig. 7), and $N_{e_2}^{\alpha}(\xi, \eta)$ is the extrapolated basis function of element e_2 at a point \mathbf{x} of element e_1 . Note that e_1 and e_2 should belong to the same patch and some basis functions of element e_2 are equal to 0 at point \mathbf{x} .

This approach may not work for some complex trimmed problems, e.g., a patch trimmed by multiple curves that results in none of the neighboring elements to the target trimmed element being suitable for extrapolation. Future

Fig. 7 An example of trimming effect



research will develop more robust strategies for addressing this issue.

4.4 Implementation

To evaluate the equation system Eq. (15) using the nonsingular BIE, Eqs. (16), (17), (37), (43) are substituted into Eq. (22) to obtain the BIE with respect to the displacements and tractions of the control points

$$\begin{aligned}
 & \sum_{e=1}^M \int_{\Gamma_e} T_{lm}(s, \mathbf{x}) N_\alpha(\mathbf{x}) u_m^\alpha(\mathbf{x}) d\Gamma(\mathbf{x}) - N_\alpha(s) u_m^\alpha(s) \\
 & \sum_{e=1}^M \int_{\Gamma_e} T_{lm}(s, \mathbf{x}) d\Gamma(\mathbf{x}) - (A_{mnj\alpha} u_j^\alpha(s) + B_{mnj\alpha} t_j^\alpha(s)) \\
 & \sum_{e=1}^M \int_{\Gamma_e} T_{lm}(s, \mathbf{x}) x(\mathbf{x})_n d\Gamma(\mathbf{x}) \\
 & + (A_{mnj\alpha} u_j^\alpha(s) + B_{mnj\alpha} t_j^\alpha(s)) x(s)_n \\
 & \sum_{e=1}^M \int_{\Gamma_e} T_{lm}(s, \mathbf{x}) d\Gamma(\mathbf{x}) \\
 & = \sum_{e=1}^M \int_{\Gamma_e} U_{lm}(s, \mathbf{x}) N_\alpha(\mathbf{x}) t_m^\alpha(\mathbf{x}) d\Gamma(\mathbf{x}) \\
 & - (C_{mnj\alpha} u_j^\alpha(s) + D_{mnj\alpha} t_j^\alpha(s)) \\
 & \sum_{e=1}^M \int_{\Gamma_e} U_{lm}(s, \mathbf{x}) n_n(\mathbf{x}) d\Gamma(\mathbf{x}). \tag{32}
 \end{aligned}$$

Note that the terms taken outside of the integrals simplify the implementation.

The first terms of left hand side and right hand side (called *field point term* for short) in Eq. (32) are computed in each element and then assembled into left hand side or right hand side of the equation system Eq. (15) according to whether $u_m^\alpha(\mathbf{x})$ and $t_m^\alpha(\mathbf{x})$ are unknown or known. Except for the first terms, all the other terms (called *source point term* for short) consist of a polynomial with respect to the displacements and tractions of source points (collocation points) and an integral with respect to the field points. The integrals are evaluated over each element and summed to get the integral over the entire boundary Γ . The integrals are then multiplied by the appropriate polynomial terms and assembled into the equation system according to $u_j^\alpha(s)$ and $t_j^\alpha(s)$.

The trimming operations may generate control points with basis functions that have zero support on the final trimmed problem domain (see the inactive control points in Fig. 8). These control points should be identified and eliminated from the computation, and the collocation points corresponding to them (such as Fig. 5) should be also ignored.

Nonsingular does not mean that the gradients of the integrands are small, or that lower order Gauss integration will accurately evaluate the integrals. The element sub-division method [41] is therefore used to accurately evaluate the integral when the source and integration points are in the same element (Fig. 9a), and for a trimmed element, the integral of the trimmed element is the difference between the integral over the untrimmed element and region outside of the trim curve as shown in Fig. 9b.

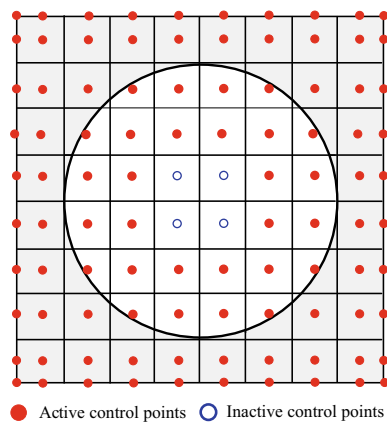


Fig. 8 Active and inactive control *points*. The knot vectors in both parametric direction are $\Xi = [0, 0, 0, 1/8, 1/4, 3/8, 1/2, 5/8, 3/4, 7/8, 1, 1, 1]$

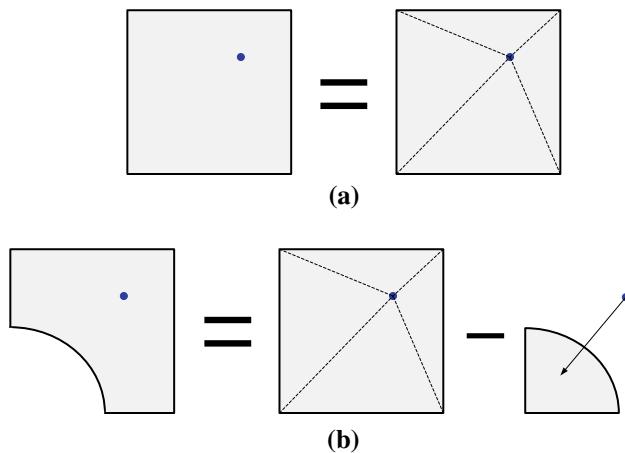


Fig. 9 Integration schemes of the source and integration *points* in the same **a** untrimmed element and **b** trimmed element

The procedure of the multi-patch nonsingular IGABEM using trimmed elements is illustrated in Fig. 10.

5 Numerical examples

All examples in the section were run on a desktop workstation with an Intel core i7 960 3.2GHz and 12GB of RAM. The OS is Linux Ubuntu 12.04, and the compiler is gfortran. The 8×8 Gauss quadrature rule is used for the integration of the untrimmed elements in terms of the discussion by Heltai et al. [29]. The quadrature design method in Sect. 3 is used for the integration of the trimmed elements; and the nearly singular integration scheme in Sect. 4.2.2 is used if the integration is nearly singular. The collocation point shift coefficient β mentioned in Sect. 4.2.3 is set to 0.5, which performs best in our tests.

5.1 Cube with a cylindrical cutout

A unit cube with a cylindrical cutout consisting of 10 patches (6 for the cubic surfaces and 4 for the cylindrical surfaces) is subjected to a perpendicular traction T on its top surface. The top and the bottom surfaces are trimmed by a circle with a diameter of 0.4. The model and the boundary conditions are illustrated in Fig. 11. Young's modulus, E , is 10^4 , and the Poisson's ratio, ν , is 0.3. In this model, the analytical solutions of the displacement in x , y and z direction of a point s on the boundary surfaces are $T\nu/E \cdot x(s)$, $T\nu/E \cdot y(s)$ and $T\nu/E \cdot z(s)$, and the stress in z direction is T .

Meshes of 2×2 , 4×4 , 6×6 and 8×8 quadratic and cubic ($p = 2$ and 3) 2D NURBS boundary elements for each trimmed patch are used in the computations and shown in Fig. 12, where the cylindrical surface is divided into four patches consisting of 1×2 , 2×4 , 3×6 and 4×8 elements. The knot vector spans are equally spaced in each direction. Twelve points along the trimming curve are selected to enforce the displacement continuity with Lagrange multipliers as shown in Fig. 14a. Only the mean relative error and the maximum relative error (shortened to the mean error and max error below) of the displacement components in Table 1 (excluding the mesh points in the trimmed domain) are included in the error norms since the other displacement components are assigned as boundary conditions. When a point is shared by several surfaces, only the common displacement components of those surfaces in Table 1 are compared.

Denoting h as the characteristic size of the elements and h_0 as the characteristic size of Mesh 1 (see Fig. 12a), the discretization ratio h/h_0 ranges from 1 to 0.25 for Meshes 1–4, and the corresponding mean and the max errors of the displacements are shown in Fig. 13. The results show that refinement improves the numerical accuracy and a higher accuracy is achieved for the elements of the same size as p increases. The result for $p = 2$ violates the convergence trend when $h/h_0 = 0.25$. The primary reason for this is the number of points enforcing the continuity must increase with the mesh refinement because the number of control points corresponding to the intersecting curves will increase with the mesh refinement. Given two intersecting patches of degree p , the expected number of control points on each patch for constraining a point is expected to be less than or equal to $(p + 1)^2$. However, too many constraints may result in an over constrained problem since the number of constraints is larger than that of the associated control points. In our experience, when the number of constraints is greater than twice of the number of associated control points, the over constrained problems may occur. A detailed discussion about the relationship between the accuracy and the number of coupled points is presented as follows.

Meshes 1 and 4 of $p = 2$ are chosen as examples to evaluate the impact of the number of coupled points on

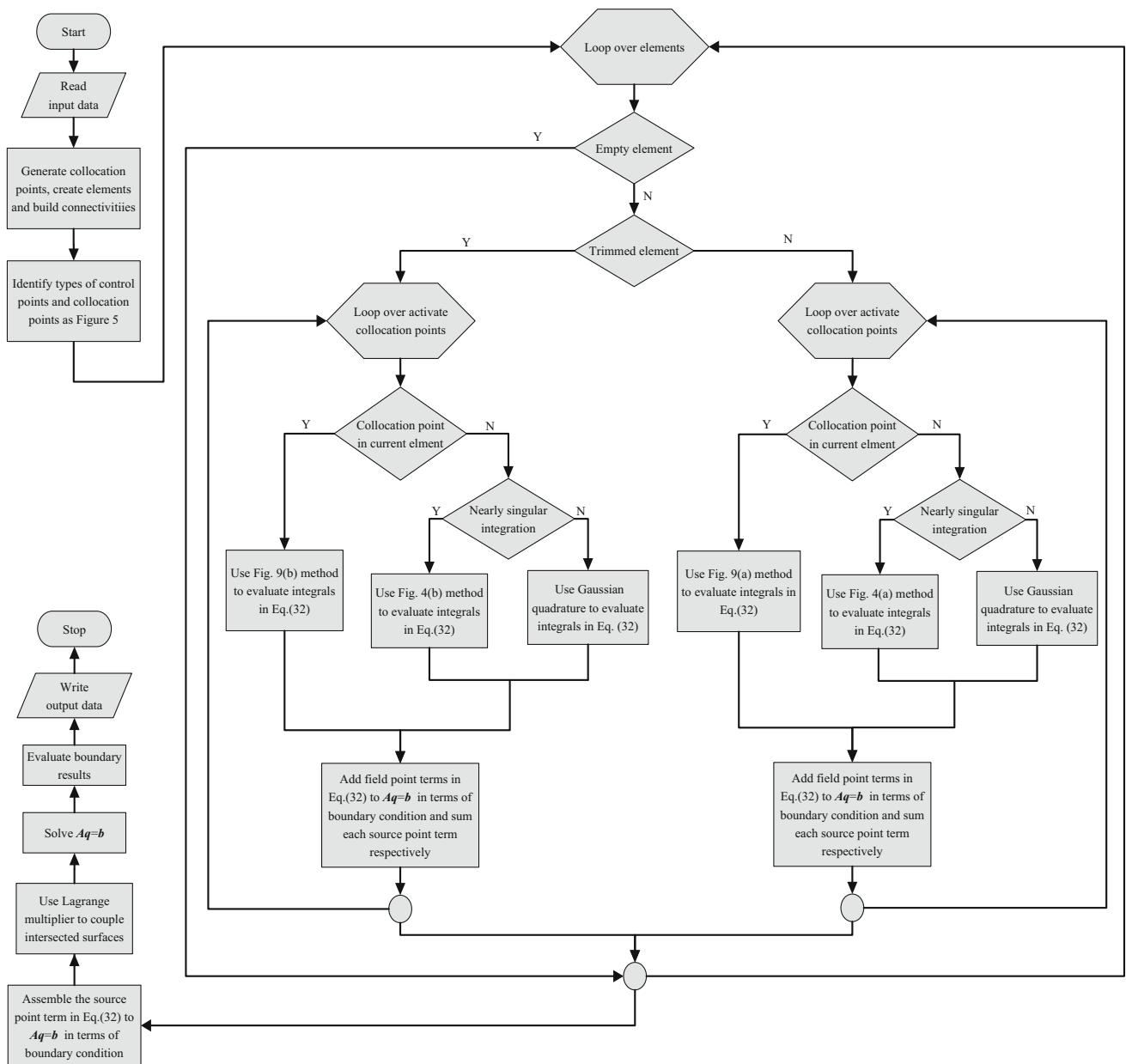
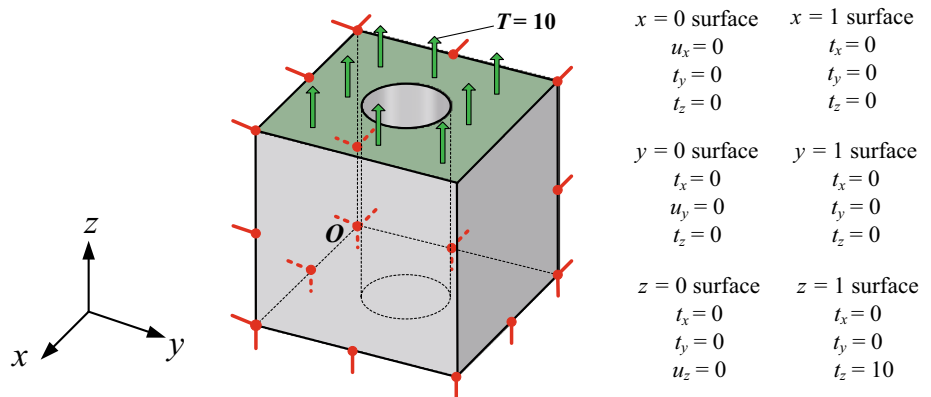


Fig. 10 Flowchart of the multi-patch nonsingular IGABEM using trimmed elements

Fig. 11 A unit cube with a cylindrical cutout



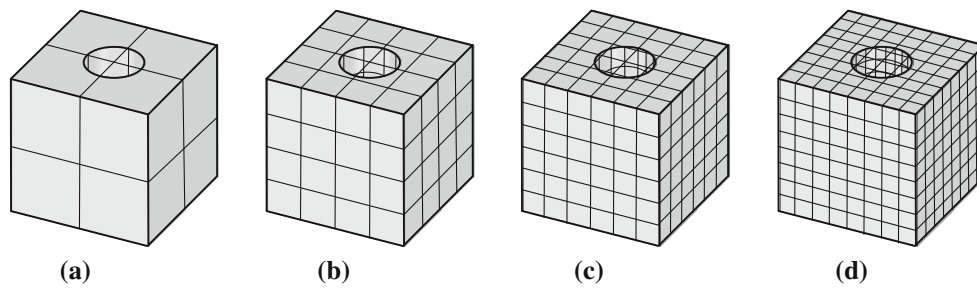


Fig. 12 Meshes of the cube model with a cylindrical cutout

Table 1 Compared displacement components of different surfaces

$x = 0$ surface	$x = 1$ surface	$y = 0$ surface	$y = 1$ surface	$z = 0$ surface	$z = 1$ surface
	u_x	u_x	u_x	u_x	u_x
u_y	u_y		u_y	u_y	u_y
u_z	u_z	u_z	u_z		u_z

the accuracy. Figure 14 gives four different coupled point distributions from sparse to dense, and Fig. 15 shows the corresponding mean and max errors. When the distribution of coupled points is sparse, increasing the number of coupled points improves the accuracy until the number reaches a cer-

tain point. Increasing the number of coupled points further will not improve the accuracy, and even may a little lower it. In Sect. 4.2.4, it was estimated that the number of coupled points may be set in the range from $0.5max(A, B)$ to $max(A, B)$, where A and B are the number of control points that influence the intersection curve of master surface and slave surface, respectively. As shown in Fig. 15, 36 coupled points are enough to guarantee the overall accuracy of the solution (each patch of the cylindrical surface has 9 control points influencing a quarter of the trimming circle).

The displacement results for Mesh 4 with $p = 2$ and 36 coupled points per trimming curve (Fig. 14c) are shown in Fig. 16, where the number of control points is 688 and the

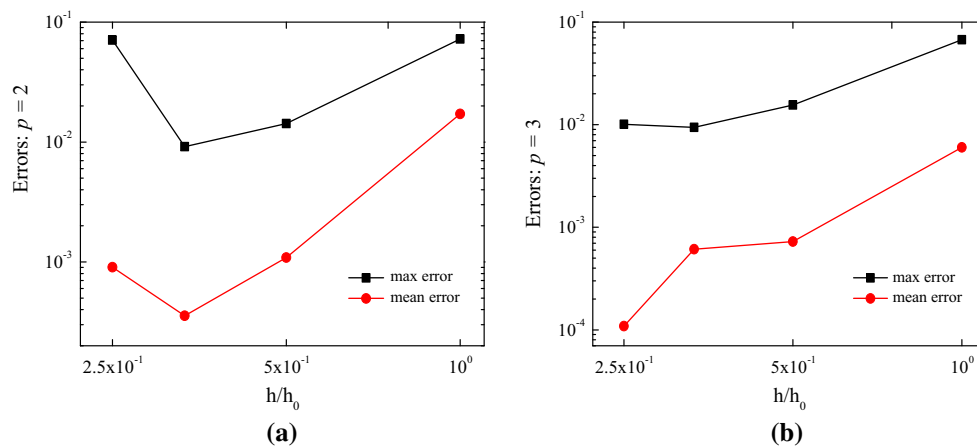


Fig. 13 Errors versus characteristic mesh parameter

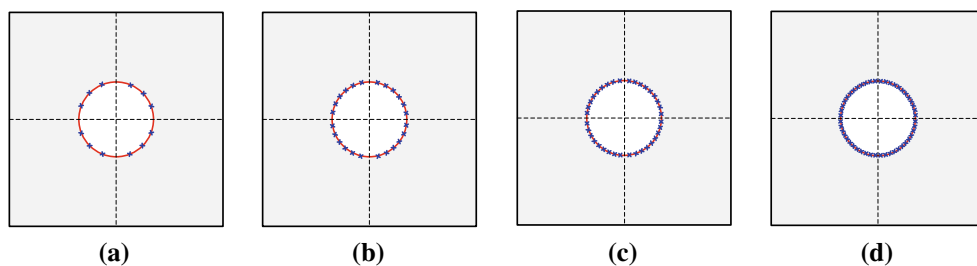


Fig. 14 Coupled points along the trimming curve

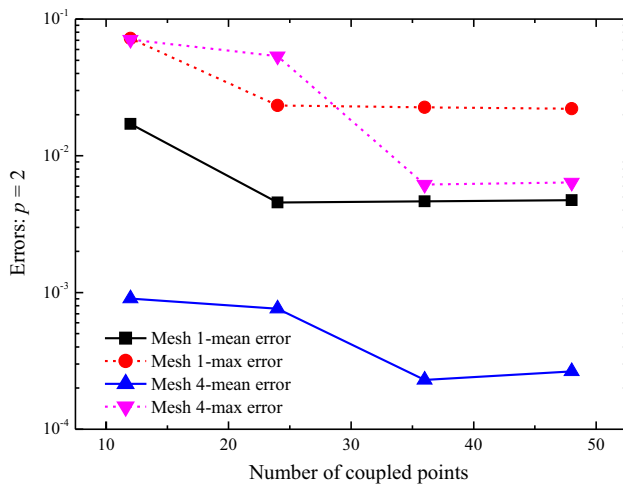


Fig. 15 Errors of different coupled point distribution

number of elements is 512. The mean error and the max error between the results of the nonsingular IGABEM with trimmed elements and the analytical solutions are $2.298 \times$

10^{-4} and 6.153×10^{-3} . Note that their percent error are approximately 0.02 and 0.6%, respectively, which proves the high degree of accuracy with the nonsingular IGABEM formulation.

5.2 Error analysis of the trimming effect

A unit cube with a cuboid cutout (see Fig. 17) is a convenient model problem for analyzing the trimming effect. The boundary conditions and material parameters are the same as the model in Fig. 11. Note that Fig. 17c is actually the example in Fig. 7. The displacements of the selected control points A–trimming effect. Of particular interest is how the errors vary with the thickness ratio l/l_0 of the trimmed elements at control points A–F.

In contrast to the other calculations, *linear* basis functions are used in this example to demonstrate that the trimming effect is not caused by the use of the NURBS basis functions in IGA. The displacements at the nodes are therefore the nodal values of the displacements, unlike in the other examples using quadratic and higher degree NURBS.

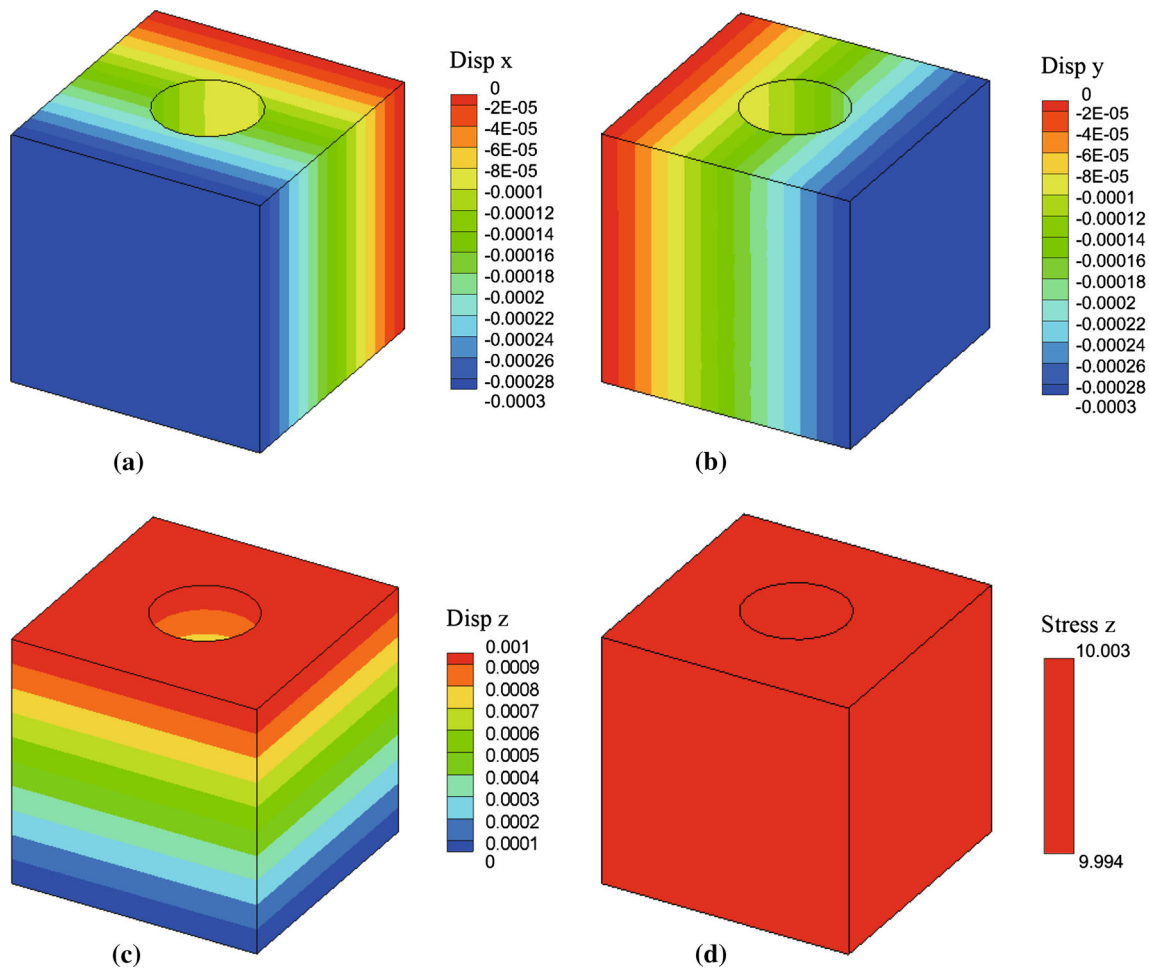


Fig. 16 Results of the *cube* with a cylindrical cutout, using quadratic elements ($p = 2$) and 36 coupled points per trimming curve

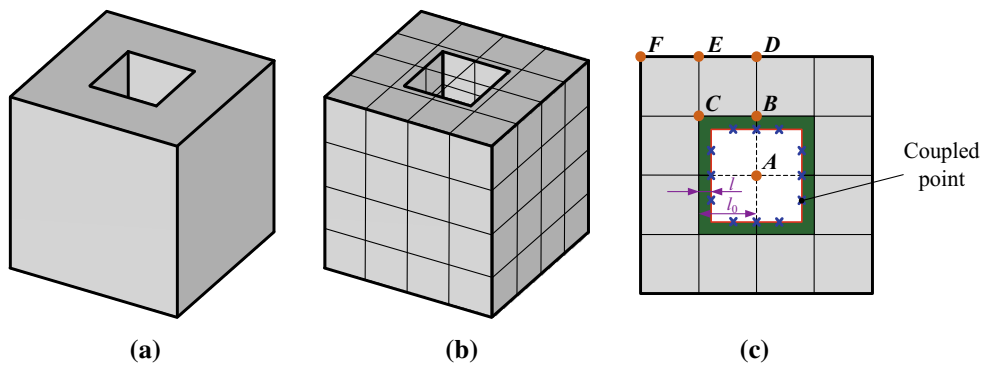


Fig. 17 An unit cube with a cuboid cutout: **a** CAD model, **b** mesh model with linear elements ($p = 1$), and **c** top surface and 12 coupled points along the trimming curve

Table 2 Relative errors of selected points with respect to different thickness ratio l/l_0

l/l_0	A	B	C	D	E	F
1/2	1.693×10^{-4}	2.500×10^{-4}	5.018×10^{-4}	1.284×10^{-3}	1.774×10^{-3}	2.096×10^{-3}
1/3	5.370×10^{-4}	1.154×10^{-4}	8.931×10^{-5}	9.447×10^{-4}	3.734×10^{-4}	1.760×10^{-4}
1/5	1.659×10^{-4}	9.833×10^{-5}	4.766×10^{-5}	2.385×10^{-4}	1.262×10^{-4}	8.259×10^{-5}
1/15	1.929×10^{-2}	2.681×10^{-3}	2.803×10^{-3}	2.227×10^{-3}	3.013×10^{-3}	3.164×10^{-3}
1/75	1.457	2.564×10^{-2}	3.768×10^{-2}	2.380×10^{-2}	2.034×10^{-2}	4.001×10^{-2}

These results were obtained without using extrapolation from the interior elements

Table 2 shows the relative errors of the selected control points with respect to different thickness ratio (l/l_0 in Fig. 7) from 1/2 to 1/75. In this example, when the relative error magnitude is or less than 10^{-3} , it is on the order of the error in the rest of the domain. When the thickness ratio becomes small, e.g., $l/l_0 = 1/15$, the displacement of control point A is 1.929×10^{-2} , which is considerably larger than the overall magnitude of the error.

For the case $l/l_0 = 1/75$ in Table 2, the extrapolation method reduces the relative errors of points B–F to 3.860×10^{-3} , 9.647×10^{-3} , 1.333×10^{-3} , 4.342×10^{-3} and 5.983×10^{-3} , respectively. Compared to the results in Table 2, the errors from the IGABEM with the extrapolation method are obviously smaller than that without it, demonstrating the utility of the extrapolation method. Note that the control point A did not influence the solution in any element in the IGABEM when the extrapolation is used since it is effectively removed from the computation.

5.3 Problems with multiple trimming curves

Multi-trimmed problems are those with patches containing multiple trim curves. In the multi-trimmed problems, if the trimming curves are very close, there may be multi-trimmed elements which are trimmed by more than one trimming curves. In the work of Kim et al. [37], a local refinement technique is applied recursively to divide the multi-trimmed elements into smaller sub-elements that are trimmed by at

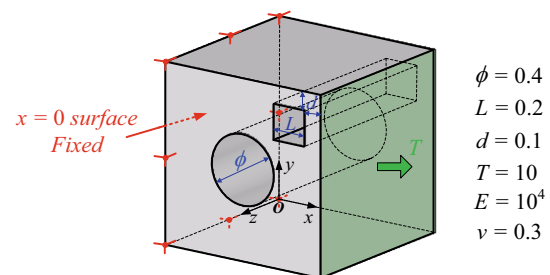


Fig. 18 An unit cube with two cutouts

most one trimming curve. However, this method is inefficient due to the extra computation introduced by the refinement. In this work, the integration of the multi-trimmed elements is directly completed by using the quadrature design method in Sect. 3, which avoids the refinement and greatly improves the efficiency. For the details about the efficiency of the quadrature design method, the reader is referred to Nagy and Benson [51].

The example in Fig. 18 is an unit cube with two cutouts where $x = 0$ surface is fixed and $x = 1$ surface is subjected uniform pressure. The entire geometry consists of 14 patches: 6 for the cube, 4 for the cylindrical cutout and 4 for the cuboid cutout. There are 24 coupled points along each circle or square trimming curve. The mesh contains 640 quadratic NURBS elements as shown in Fig. 19a and the corresponding number of control points is 888. An element which is trimmed by two curves is shown in Fig. 19b. Assuming the domain

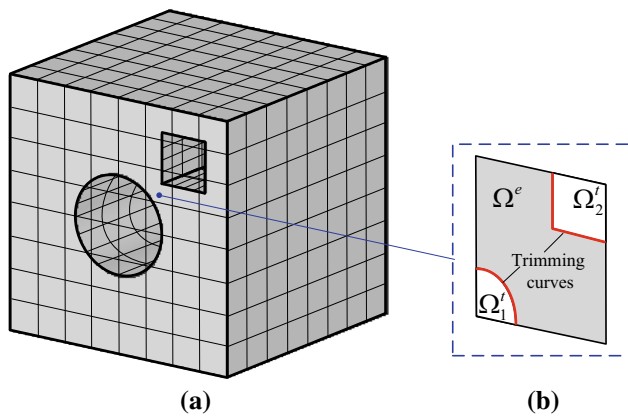


Fig. 19 The discrete model of the multi-trimmed cube in Fig. 18: **a** mesh and **b** a multi-trimmed element

of the untrimmed element is Ω_0^e , the domain of the multi-trimmed Ω^e is $\Omega_0^e - \Omega_1^i - \Omega_2^i$ where Ω_1^i and Ω_2^i are the cut-out parts. The integration points in Ω^e are obtained by using the quadrature design method once.

The von Mises stress solution of the IGABEM with multi-trimmed elements is plotted in Fig. 20a, and two ANSYS solutions using 3733 and 31,929 quadratic tetrahedral elements are shown in Fig. 20b, c, respectively. The ANSYS solution from the finer mesh is chosen as the reference solution. Based on the von Mises stress, the IGABEM solution is closer to the reference solution than the ANSYS coarse mesh solution. Note that the element size in the IGABEM and coarse mesh for ANSYS are the same, demonstrating the coarse mesh accuracy of the IGABEM.

6 Conclusions

The singular or weakly singular integrals in the BEM must be evaluated by specialized integration methods, some of which

cannot be used in the IGABEM [69], e.g., the rigid-body motion method, increasing the difficulty of implementing IGABEM. Moreover, many of the methods that are suitable for simple basis functions, such as linear triangles or bilinear quadrilaterals, are not applicable to higher order elements.

Applying the nonsingular formulation of the BEM–IGA, which was first applied to IGABEM for Stokes flows by Heltai et al. [29], is an effective method for addressing the integration issues. In this research, based on the nonsingular BEM in [47], a multi-patch nonsingular IGABEM with trimmed elements is presented. The quadrature rules for the trimmed elements are obtained from the quadrature-design method [51], which are optimal within the trimmed domains.

A modified set of Greville abscissae with the first and last points moved to the element interiors is used to locate the collocation points at the sharp edges and corners, and a simple averaging technique is adopted to merge the surplus collocation points along the edges and corners. Integration by subdivision is used along the C^0 boundaries. Lagrange multipliers are used to enforce displacement continuity along trimmed edges.

Numerical examples have demonstrated that the non-singular IGABEM with trimmed elements accurately and efficiently solves the trimmed problems, even the multi-trimmed problems. Compared to the traditional IGABEM, the IGABEM with trimmed elements may introduce errors associated with the basis functions that have their support limited to the small element fragments generated by the trimming process, and an extrapolation method is proposed to solve this trimming effect.

In order to further improve the accuracy and efficiency of the method proposed in this paper, a more robust interpolation scheme is being pursued to conquer the trimming effect, and the fast multipole BEM [76, 78] is planned to replace the conventional BEM in the IGA to accelerate the integration computation. Besides that, other patch-coupling methods, e.g., Nitsche’s method [52, 61], Mortar method etc. [14, 20],

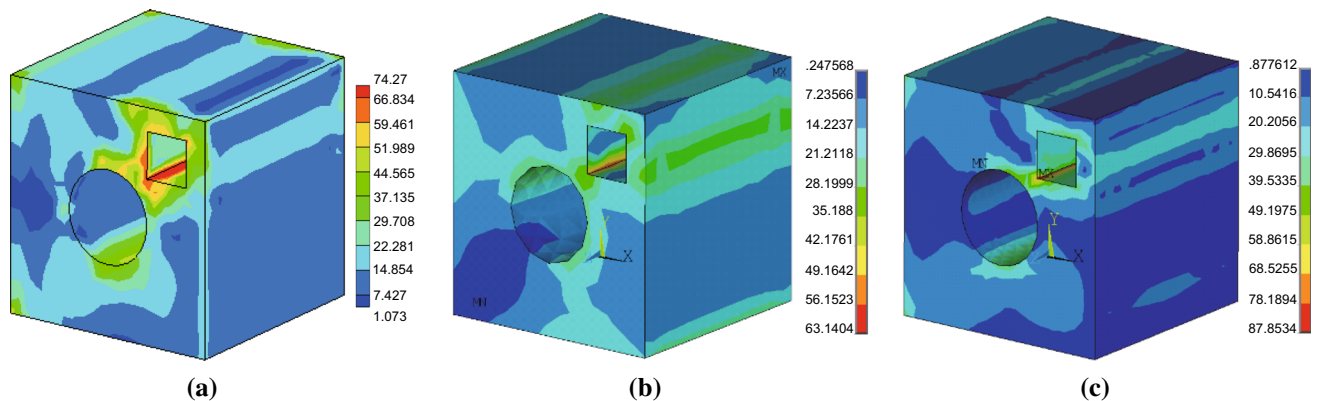


Fig. 20 The von Mises stress solutions of the multi-trimmed cube: **a** IGABEM with quadratic NURBS elements, **b** ANSYS with 3733 quadratic tetrahedral elements and **c** ANSYS with 31,929 quadratic tetrahedral elements

will be tried, and the nonsingular IGABEM with trimmed elements will be expanded to other engineering problems, such as elastodynamics, fluid mechanics and acoustics.

Acknowledgments The support for this research and Yingjun Wang by NSF Grant CMMI-1068106 is gratefully acknowledged.

Appendix: Evaluation of boundary stresses and displacement gradients

The boundary stresses in the IGABEM may be derived from the traction-recovery method [24]. Following their development, a local Cartesian coordinate system \bar{x}_i is defined as shown in Fig. 21 (global coordinate system is x_i), where \bar{x}_1 and \bar{x}_2 are tangential to the surface and \bar{x}_3 is directed in the outward normal direction. In order to concisely describe the formulation, the notation (ξ_1, ξ_2) replaces (ξ, η) for the intrinsic coordinates.

The derivatives of the intrinsic coordinates are

$$\frac{\partial \xi_1}{\partial \bar{x}_1} = \frac{1}{m_1}, \quad \frac{\partial \xi_1}{\partial \bar{x}_2} = \frac{-\cos \theta}{|m_1| \sin \theta}, \quad \frac{\partial \xi_2}{\partial \bar{x}_1} = 0, \quad \frac{\partial \xi_2}{\partial \bar{x}_2} = \frac{1}{|m_2| \sin \theta}, \tag{33}$$

where m_k and the angle θ are given as

$$|m_k| = \sqrt{\left(\frac{\partial x_1}{\partial \xi_k}\right)^2 + \left(\frac{\partial x_2}{\partial \xi_k}\right)^2 + \left(\frac{\partial x_3}{\partial \xi_k}\right)^2}, \quad \cos \theta = \frac{1}{|m_1||m_2|} \frac{\partial x_i}{\partial \xi_1} \frac{\partial x_i}{\partial \xi_2}. \tag{34}$$

The local displacements and tractions are expressed in terms of the global displacements and tractions

$$\bar{u}_i = L_{ij} u_j, \quad \bar{t}_i = L_{ij} t_j, \tag{35}$$

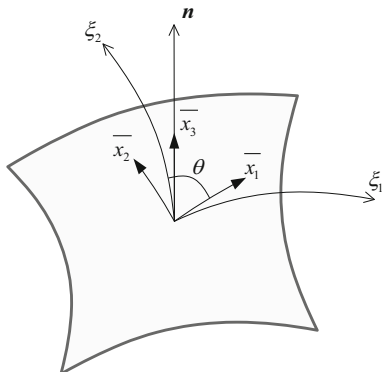


Fig. 21 Local orthogonal system for evaluating the derivatives of displacements

in which L_{ij} are entries of the rotation matrix L

$$L = \begin{bmatrix} \frac{1}{|m_1|} \frac{\partial x_1}{\partial \xi_1} & \frac{1}{|m_1|} \frac{\partial x_2}{\partial \xi_1} & \frac{1}{|m_1|} \frac{\partial x_3}{\partial \xi_1} \\ n_2 L_{13} - n_3 L_{12} & n_3 L_{11} - n_1 L_{13} & n_1 L_{12} - n_2 L_{11} \\ n_1 & n_2 & n_3 \end{bmatrix}, \tag{36}$$

where $n_1, n_2,$ and n_3 are the components of unit outward normal.

After some lengthy algebra using Hooke’s law, the boundary stress may be expressed in terms of the displacements and tractions of control points as

$$\sigma_{mn} = C_{mnj\alpha} u_j^\alpha + D_{mnj\alpha} t_j^\alpha, \tag{37}$$

where the coefficients $C_{mnj\alpha}$ and $D_{mnj\alpha}$ are

$$C_{mnj\alpha} = 2\mu \left\{ \frac{1}{1-\nu} \left[L_{1m} L_{1n} \left(\frac{\partial \xi_k}{\partial \bar{x}_1} L_{1j} + \nu \frac{\partial \xi_k}{\partial \bar{x}_2} L_{2j} \right) + L_{2m} L_{2n} \left(\frac{\partial \xi_k}{\partial \bar{x}_2} L_{2j} + \nu \frac{\partial \xi_k}{\partial \bar{x}_1} L_{1j} \right) \right] + \frac{1}{2} (L_{1m} L_{2n} + L_{2m} L_{1n}) \left(\frac{\partial \xi_k}{\partial \bar{x}_1} L_{2j} + \frac{\partial \xi_k}{\partial \bar{x}_2} L_{1j} \right) \right\} \frac{\partial N_\alpha}{\partial \xi_k}, \tag{38}$$

$$D_{mnj\alpha} = (L_{3m} L_{1n} + L_{1m} L_{3n}) L_{1j} + (L_{2m} L_{3n} + L_{3m} L_{2n}) L_{2j} + \left(\frac{\nu}{1-\nu} \delta_{mn} + \frac{1-2\nu}{1-\nu} L_{3m} L_{3n} \right) L_{3j}, \tag{39}$$

where N_α is the basis function associated with the α th control point of the element [refer to Eqs. (16) and (17)], ν is Poisson’s ratio, μ is shear modulus, and δ_{ij} is Kronecker delta.

With the help of the local coordinate system in Fig. 21, the derivatives of global displacement can be expressed as

$$u_{m,n} = L_{rm} L_{sn} \bar{u}_{r,s}. \tag{40}$$

When the subscript j does not equal 3, the local derivatives of displacements are

$$\bar{u}_{i,j} = \frac{\partial \bar{u}_i}{\partial \bar{x}_j} = \frac{\partial \bar{u}_i}{\partial \xi_k} \frac{\partial \xi_k}{\partial \bar{x}_j}, \tag{41}$$

where the subscript k ranges from 1 to 2. When the subscript j equals to 3, according to Hooke’s law and $\bar{\sigma}_{i3} = \bar{t}_i$, the local derivatives of the displacements are

$$\begin{aligned} \frac{\partial \bar{u}_1}{\partial \bar{x}_3} &= \frac{\bar{t}_1}{\mu} - \left(\frac{\partial \bar{u}_3}{\partial \xi_k} \frac{\partial \xi_k}{\partial \bar{x}_1} \right), \\ \frac{\partial \bar{u}_2}{\partial \bar{x}_3} &= \frac{\bar{t}_2}{\mu} - \left(\frac{\partial \bar{u}_3}{\partial \xi_k} \frac{\partial \xi_k}{\partial \bar{x}_2} \right), \\ \frac{\partial \bar{u}_3}{\partial \bar{x}_3} &= \frac{1-2\nu}{\mu(2-2\nu)} \bar{t}_3 - \frac{\nu}{1-\nu} \left(\frac{\partial \bar{u}_1}{\partial \xi_k} \frac{\partial \xi_k}{\partial \bar{x}_1} + \frac{\partial \bar{u}_2}{\partial \xi_k} \frac{\partial \xi_k}{\partial \bar{x}_2} \right). \end{aligned} \tag{42}$$

Using Eqs. (16), (17), (35), (40)–(42), the derivatives of displacements are expressed in terms of the displacements and tractions of control points

$$u_{m,n} = A_{mnj\alpha} u_j^\alpha + B_{mnj\alpha} t_j^\alpha, \tag{43}$$

where the coefficient $A_{mnj\alpha}$ is

$$\begin{aligned} A_{mnj\alpha} &= (L_{1m}L_{1j} + L_{2m}L_{2j} + L_{3m}L_{3j}) L_{1n}c_{\alpha 1} \\ &+ \left(\frac{\nu}{\nu-1} L_{3m} + L_{1j} - L_{1m}L_{3j} \right) L_{3n}c_{\alpha 1} \\ &+ (L_{1m}L_{1j} + L_{2m}L_{2j} + L_{3m}L_{3j}) L_{2n}c_{\alpha 2} \\ &+ \left(\frac{\nu}{\nu-1} L_{3m} + L_{2j} - L_{2m}L_{3j} \right) L_{3n}c_{\alpha 2}, \end{aligned} \tag{44}$$

where coefficients $c_{\alpha 1}$ and $c_{\alpha 2}$ are

$$c_{\alpha 1} = \frac{\partial \xi_1}{\partial \bar{x}_1} \frac{\partial N_\alpha}{\partial \xi_1} + \frac{\partial \xi_2}{\partial \bar{x}_1} \frac{\partial N_\alpha}{\partial \xi_2}, \tag{45}$$

$$c_{\alpha 2} = \frac{\partial \xi_1}{\partial \bar{x}_2} \frac{\partial N_\alpha}{\partial \xi_1} + \frac{\partial \xi_2}{\partial \bar{x}_2} \frac{\partial N_\alpha}{\partial \xi_2}, \tag{46}$$

and the coefficient $B_{mnj\alpha}$ is

$$\begin{aligned} B_{mnj\alpha} &= \frac{L_{3n}}{\mu} \left(L_{1m}L_{1j} + L_{2m}L_{2j} \right. \\ &\left. + \frac{1-2\nu}{2(1-\nu)} L_{3m}L_{3j} \right) N_\alpha. \end{aligned} \tag{47}$$

References

1. Akkerman I, Bazilevs Y, Kees CE, Farthing MW (2011) Isogeometric analysis of free-surface flow. *J Comput Phys* 230(11):4137–4152
2. Azegami H, Fukumoto S, Aoyama T (2013) Shape optimization of continua using NURBS as basis functions. *Struct Multidiscip Optim* 47(2):247–258
3. Banerjee PK, Butterfield R (1978) *The boundary element method for engineers*, vol 17. Pentech Press, London
4. Banerjee PK, Butterfield R (1981) *Boundary element methods in engineering science*, vol 17. McGraw-Hill, London
5. Bazilevs Y, Calo VM, Cottrell JA, Evans JA, Hughes TJR, Lipton S, Scott MA, Sederberg TW (2010) Isogeometric analysis using T-splines. *Comput Methods Appl Mech Eng* 199(5):229–263

6. Bazilevs Y, Hsu MC, Scott MA (2012) Isogeometric fluid–structure interaction analysis with emphasis on non-matching discretizations, and with application to wind turbines. *Comput Methods Appl Mech Eng* 249:28–41
7. Bazilevs Y, Michler C, Calo VM, Hughes TJR (2010) Isogeometric variational multiscale modeling of wall-bounded turbulent flows with weakly enforced boundary conditions on unstretched meshes. *Comput Methods Appl Mech Eng* 199(13):780–790
8. Bazilevs Y, Takizawa K, Tezduyar TE, Hsu MC, Kostov N, McIntyre S (2014) Aerodynamic and FSI analysis of wind turbines with the ALE-VMS and ST-VMS methods. *Arch Comput Methods Eng* 21(4):359–398
9. Beer G, Smith I, Duenser C (2008) *The boundary element method with programming: for engineers and scientists*. Springer, Berlin
10. Benson DJ, Bazilevs Y, Hsu M-C, Hughes TJR (2010) Isogeometric shell analysis: the Reissner–Mindlin shell. *Comput Methods Appl Mech Eng* 199:276–289
11. Benson DJ, Bazilevs Y, Hsu M-C, Hughes TJR (2011) A large deformation, rotation-free, isogeometric shell. *Comput Methods Appl Mech Eng* 200:1367–1378
12. Benson DJ, Hartmann S, Bazilevs Y, Hsu M-C, Hughes TJR (2013) Blended isogeometric shells. *Comput Methods Appl Mech Eng* 255:133–146
13. Borden MJ, Verhoosel CV, Scott MA, Hughes TJR, Landis CM (2012) A phase-field description of dynamic brittle fracture. *Comput Methods Appl Mech Eng* 217:77–95
14. Brivadis E, Buffa A, Wohlmuth B, Wunderlich L (2015) Isogeometric mortar methods. *Comput Methods Appl Mech Eng* 284:292–319
15. Buffa A, Sangalli G, Vázquez R (2014) Isogeometric methods for computational electromagnetics: B-spline and T-spline discretizations. *J Comput Phys* 257:1291–1320
16. Cottrell JA, Hughes TJR, Bazilevs Y (2009) *Isogeometric analysis: toward integration of CAD and FEA*. Wiley, Chichester
17. Cottrell JA, Reali A, Bazilevs Y, Hughes TJR (2006) Isogeometric analysis of structural vibrations. *Comput Methods Appl Mech Eng* 195(41):5257–5296
18. De Luycker E, Benson DJ, Belytschko T, Bazilevs Y, Hsu M-C (2011) X-FEM in isogeometric analysis for linear fracture mechanics. *Int J Numer Methods Eng* 87:541–565
19. Dedè L, Borden MJ, Hughes TJR (2012) Isogeometric analysis for topology optimization with a phase field model. *Arch Comput Methods Eng* 19(3):427–465
20. Dittmann M, Franke M, Temizer İ, Hesch C (2014) Isogeometric Analysis and thermomechanical Mortar contact problems. *Comput Methods Appl Mech Eng* 274:192–212
21. Felippa CA (2004) *Introduction to finite element methods*. University of Colorado, Boulder. <http://www.colorado.edu/engineering/CAS/courses.d/IFEM.d>
22. Gao XW (2002) The radial integration method for evaluation of domain integrals with boundary-only discretization. *Eng Anal Bound Elem* 26(10):905–916
23. Gao XW (2010) An effective method for numerical evaluation of general 2D and 3D high order singular boundary integrals. *Comput Methods Appl Mech Eng* 199(45):2856–2864
24. Gao XW, Davies TG (2002) *Boundary element programming in mechanics*. Cambridge University Press, Cambridge
25. Ginnis AI, Kostas KV, Politis CG, Kaklis PD, Belibassakis KA, Gerostathis ThP, Scott MA, Hughes TJR (2014) Isogeometric boundary-element analysis for the wave-resistance problem using T-splines. *Comput Methods Appl Mech Eng* 279:425–439
26. Gu JL, Zhang JM, Li GY (2012) Isogeometric analysis in BIE for 3-D potential problem. *Eng Anal Bound Elem* 36(5):858–865
27. Guiggiani M, Gigante A (1990) A general algorithm for multidimensional Cauchy principal value integrals in the boundary element method. *J Appl Mech* 57(4):906–915

28. Guiggiani M, Krishnasamy G, Rudolphi TJ, Rizzo FJ (1992) A general algorithm for the numerical solution of hypersingular boundary integral equations. *J Appl Mech* 59(3):604–614
29. Heltai L, Arroyo M, DeSimone A (2014) Nonsingular isogeometric boundary element method for Stokes flows in 3D. *Comput Methods Appl Mech Eng* 268:514–539
30. Speleers H, Manni C, Pelosi F (2013) From NURBS to NURPS geometries. *Comput Methods Appl Mech Eng* 255:238–254
31. Speleers H, Manni C, Pelosi F, Sampoli ML (2012) Isogeometric analysis with Powell–Sabin splines for advection–diffusion–reaction problems. *Comput Methods Appl Mech Eng* 221:132–148
32. Hsu MC, Bazilevs Y (2012) Fluid–structure interaction modeling of wind turbines: simulating the full machine. *Comput Mech* 50(6):821–833
33. Hughes TJR, Cottrell JA, Bazilevs Y (2005) Isogeometric analysis: CAD, finite elements, NURBS, exact geometry, and mesh refinement. *Comput Methods Appl Mech Eng* 194:4135–4195
34. Hughes TJR (2000) *The finite element method: linear static and dynamic finite element analysis*. Courier Dover Publications, New York
35. Johnston PR, Elliott D (2005) A sinh transformation for evaluating nearly singular boundary element integrals. *Int J Numer Methods Eng* 62(4):564–578
36. Kane JH, Gupta A, Saigal S (1989) Reusable intrinsic sample point (RISP) algorithm for the efficient numerical integration of three dimensional curved boundary elements. *Int J Numer Methods Eng* 28(7):1661–1676
37. Kim HJ, Seo YD, Youn SK (2009) Isogeometric analysis for trimmed CAD surfaces. *Comput Methods Appl Mech Eng* 198(37):2982–2995
38. Kim HJ, Seo YD, Youn SK (2010) Isogeometric analysis with trimming technique for problems of arbitrary complex topology. *Comput Methods Appl Mech Eng* 199(45):2796–2812
39. Klaseboer E, Fernandez CR, Khoo BC (2009) A note on true desingularisation of boundary integral methods for three-dimensional potential problems. *Eng Anal Bound Elem* 33(6):796–801
40. Klaseboer E, Sun Q, Chan DYC (2012) Non-singular boundary integral methods for fluid mechanics applications. *J Fluid Mech* 696:468–478
41. Lachat JC, Watson JO (1976) Effective numerical treatment of boundary integral equations: a formulation for three-dimensional elastostatics. *Int J Numer Methods Eng* 10(5):991–1005
42. Lasserre J (1998) Integration on a convex polytope. *Proc Am Math Soc* 126(8):2433–2441
43. Li K, Qian XP (2011) Isogeometric analysis and shape optimization via boundary integral. *Comput Aided Des* 43(11):1427–1437
44. Liu J, Dedè L, Evans JA, Borden MJ, Hughes TJR (2013) Isogeometric analysis of the advective Cahn–Hilliard equation: spinodal decomposition under shear flow. *J Comput Phys* 242:321–350
45. Liu YJ (2000) On the simple-solution method and non-singular nature of the BIE/BEM—a review and some new results. *Eng Anal Bound Elem* 24(10):789–795
46. Liu YJ, Rudolphi TJ (1991) Some identities for fundamental solutions and their applications to weakly-singular boundary element formulations. *Eng Anal Bound Elem* 8(6):301–311
47. Liu YJ, Rudolphi TJ (1999) New identities for fundamental solutions and their applications to non-singular boundary element formulations. *Comput Mech* 24(4):286–292
48. De Lorenzis L, Temizer I, Wriggers P, Zavarise G (2011) A large deformation frictional contact formulation using NURBS-based isogeometric analysis. *Int J Numer Methods Eng* 87:1278–1300
49. Lv JH, Miao Y, Zhu HP (2014) The distance sinh transformation for the numerical evaluation of nearly singular integrals over curved surface elements. *Comput Mech* 53(2):359–367
50. Ma H, Kamiya N (2002) Distance transformation for the numerical evaluation of near singular boundary integrals with various kernels in boundary element method. *Eng Anal Bound Elem* 26(4):329–339
51. Nagy AP, Benson DJ (2015) On the numerical integration of trimmed isogeometric elements. *Comput Methods Appl Mech Eng* 284:165–185
52. Nguyen VP, Kerfriden P, Brino M, Bordas SPA, Bonisoli E (2014) Nitsches method for two and three dimensional NURBS patch coupling. *Comput Mech* 53(6):1163–1182
53. Nguyen-Thanh N, Kiendl J, Nguyen-Xuan H, Wüchner R, Bletzinger KU, Bazilevs Y, Rabczuk T (2011) Rotation free isogeometric thin shell analysis using PHT-splines. *Comput Methods Appl Mech Eng* 200(47):3410–3424
54. Niu ZR, Wendland WL, Wang XX, Zhou HL (2005) A semi-analytical algorithm for the evaluation of the nearly singular integrals in three-dimensional boundary element methods. *Comput Methods Appl Mech Eng* 194(9):1057–1074
55. Peake MJ, Trevelyan J, Coates G (2013) Extended isogeometric boundary element method (XIBEM) for two-dimensional Helmholtz problems. *Comput Methods Appl Mech Eng* 259:93–102
56. Piegl L, Tiller W (1997) *The NURBS book* (monographs in visual communication). Springer, Berlin
57. Qian XP (2010) Full analytical sensitivities in NURBS based isogeometric shape optimization. *Comput Methods Appl Mech Eng* 199(29):2059–2071
58. Raknes SB, Deng X, Bazilevs Y, Benson DJ, Mathisen KM, Kvamsdal T (2013) Isogeometric rotation-free bending-stabilized cables: statics, dynamics, bending strips and coupling with shells. *Comput Methods Appl Mech Eng* 263:127–143
59. Rizzo FJ, Shippy DJ (1977) An advanced boundary integral equation method for three-dimensional thermoelasticity. *Int J Numer Methods Eng* 11(11):1753–1768
60. Ruess M, Schillinger D, Bazilevs Y, Varduhn V, Rank E (2013) Weakly enforced essential boundary conditions for NURBS-embedded and trimmed NURBS geometries on the basis of the finite cell method. *Int J Numer Methods Eng* 95(10):811–846
61. Ruess M, Schillinger D, Özcan AI, Rank E (2014) Weak coupling for isogeometric analysis of non-matching and trimmed multi-patch geometries. *Comput Methods Appl Mech Eng* 269:46–71
62. Schillinger D, Dede L, Scott MA, Evans JA, Borden MJ, Rank E, Hughes TJR (2012) An isogeometric design-through-analysis methodology based on adaptive hierarchical refinement of NURBS, immersed boundary methods, and T-spline CAD surfaces. *Comput Methods Appl Mech Eng* 249:116–150
63. Scott MA, Borden MJ, Verhoosel CV, Sederberg TW, Hughes TJR (2011) Isogeometric finite element data structures based on Bézier extraction of T-splines. *Int J Numer Methods Eng* 88(2):126–156
64. Scott MA, Li X, Sederberg TW, Hughes TJR (2012) Local refinement of analysis-suitable T-splines. *Comput Methods Appl Mech Eng* 213:206–222
65. Scott MA, Simpson RN, Evans JA, Lipton S, Bordas SPA, Hughes TJR, Sederberg TW (2013) Isogeometric boundary element analysis using unstructured T-splines. *Comput Methods Appl Mech Eng* 254:197–221
66. Sederberg TW, Zheng J, Bakenov A, Nasri A (2003) T-splines and t-NURCCs. *ACM Trans Graph* 22(3):477–484
67. Seo YD, Kim HJ, Youn SK (2010) Isogeometric topology optimization using trimmed spline surfaces. *Comput Methods Appl Mech Eng* 199(49):3270–3296
68. Sevilla R, Fernández-Méndez S, Huerta A (2008) NURBS-enhanced finite element method (NEFEM). *Int J Numer Methods Eng* 76(1):56–83
69. Simpson RN, Bordas SPA, Trevelyan J, Rabczuk T (2012) A two-dimensional isogeometric boundary element method for elastostatic analysis. *Comput Methods Appl Mech Eng* 209:87–100

70. Takahashi T, Matsumoto T (2012) An application of fast multipole method to isogeometric boundary element method for Laplace equation in two dimensions. *Eng Anal Bound Elem* 36(12):1766–1775
71. Telles JCF (1987) A self-adaptive co-ordinate transformation for efficient numerical evaluation of general boundary element integrals. *Int J Numer Methods Eng* 24(5):959–973
72. Temizer I, Wriggers P, Hughes TJR (2012) Three-dimensional mortar-based frictional contact treatment in isogeometric analysis with NURBS. *Comput Methods Appl Mech Eng* 223–224:173–185
73. Vuong A-V, Giannelli C, Jüttler B, Simeon B (2011) A hierarchical approach to adaptive local refinement in isogeometric analysis. *Comput Methods Appl Mech Eng* 200(49):3554–3567
74. Wang YJ, Benson DJ (2015) Multi-patch nonsingular isogeometric boundary element analysis in 3D. *Comput Methods Appl Mech Eng*
75. Wang P, Xu JL, Deng JS, Chen FL (2011) Adaptive isogeometric analysis using rational PHT-splines. *Comput Aided Des* 43(11):1438–1448
76. Wang YJ, Wang QF, Wang G, Huang YB, Wang ST (2013) An adaptive dual-information FMBEM for 3D elasticity and its GPU implementation. *Eng Anal Bound Elem* 37(2):236–249
77. Wang YW, Huang ZD, Zheng Y, Zhang SG (2013) Isogeometric analysis for compound B-spline surfaces. *Comput Methods Appl Mech Eng* 261:1–15
78. Wang YJ, Wang QF, Deng XW, Xia ZH, Yan JH, Xu H (2015) Graphics processing unit (GPU) accelerated fast multipole BEM with level-skip M2L for 3D elasticity problems. *Adv Eng Softw* 82:105–118
79. Xie GZ, Zhang JM, Dong YQ, Huang C, Li GY (2014) An improved exponential transformation for nearly singular boundary element integrals in elasticity problems. *Int J Solids Struct* 51(6):1322–1329
80. Ye WJ (2008) A new transformation technique for evaluating nearly singular integrals. *Comput Mech* 42(3):457–466
81. Yun BI (2006) A generalized non-linear transformation for evaluating singular integrals. *Int J Numer Methods Eng* 65(12):1947–1969
82. Zhou HL, Niu ZR, Cheng CZ, Guan ZW (2008) Analytical integral algorithm applied to boundary layer effect and thin body effect in BEM for anisotropic potential problems. *Comput Struct* 86(15):1656–1671